ISSN: 2454-9940

INTERNATIONAL JOURNAL OF APPLIED SCIENCE ENGINEERING AND MANAGEMENT

E-Mail :
editor.ijasem@gmail.com
editor@ijasem.org

www.ijasem.org

INTERNATIONAL JOURNAL OF APPLIED SCIENCE ENGINEERING AND MANAGEMENT

ISSN2454-9940www.ijsem.org

Vol 12, Issuse.2 June 2021

A new series reversion-based Omega-K algorithm for SAR imaging with a circular trajectory scan

CHITTIMUR SRINIVASULU REDDY[1],SANDRA MUNI RAJA[2],

Abstract

In order to create CTSSAR images, a modified version of the Omega-K method is shown here. As with traditional SAR imaging techniques like RD and CS, the curvature of a circular trajectory makes it challenging to get access to the two-dimensional frequency spectrum for CTSSAR using the principle of stationary phase (POSP). To achieve precise data focus, we first use series reversion and the POSP to obtain the analytic point target spectrum, upon which we build a modified Omega-K algorithm. In order to maintain sufficient terms in the two series expansions for a suitable range approximation, one might regulate the precision. Extensive theoretical and experimental work has shown that the fourth-order approximation is the most appropriate. In addition, the suggested approach is compared to the back projection algorithm and other methods with varying estimated orders in order to gauge its computing efficiency. The computational load of the suggested method is shown to be the lowest. The suggested approach is validated by simulations, which provide sharp images.

Keywords:

Synthetic aperture radar (SAR) using a circularly sweeping trajectory (CTSSAR), series reversion, and the Omega-K method

Introduction

Synthetic aperture radar (SAR) has found widespread application in both military and civilian contexts due to its effectiveness in both day and night and all-weather situations. Typical SAR systems travel in a straight line, above or below a predetermined ground plane [1-4]. The curved path SAR has gained increasing interest among researchers in recent years. Gradually becoming one of the hotspots in the area of radar signal processing [5] is an imaging mode known as circular SAR (CSAR), whose radar equipment travels along a circular route. When the sensor is in CSAR imaging mode, the antenna beam may be directed to highlight a specific area of the ground, much like the "circular spotlight" mode of a conventional spotlight. CSAR's ability to reach subwavelength resolution in the ground plane because to its 360° aperture is only one of several benefits it offers over conventional RADAR. Furthermore, the information of the interested object from multiple azimuth directions is provided by the multi-aspect observation of CSAR, allowing for a 3D reconstruction to be realized [6-14]. Although CSAR has several benefits, the imaging area is limited. The typical ground-plane imaging region is several hundred meters in height and diameter [15]. As a result, it may be used for detailed imaging of a specific region. Many scientists are curious in the novel circular trajectory scanning SAR (CTSSAR) imaging technique [16].

ASSOCIATE PROFESSOR[1], ASSISTANT PROFESSOR[2],
DEPARTMENT OF EEE
PBR VISVODAYA INSTITUTE OF TECHNOLOGY AND SCIENCE::KAVALI

Because the platform's antenna beam is set at an angle perpendicular to the flight velocity away from the center of the circular trajectory, the resulting antenna footprint sweeps through an annular landscape as the platform travels in this mode. CTSSAR is quite similar to both the spotlight SAR and the CSAR, with the exception of the track's form, which is what sets it apart from a regular strip map. This is why we like to refer to CTSSAR as a circular strip map. CTSSAR is better suited for rapid broad area imaging despite the fact that it may need sacrificing some image detail in the azimuth direction in exchange for its faster scanning speed in azimuth compared to the conventional strip map mode. As a result of CTSSAR's curved trajectory, the target's range function contains trigonometric functions denoted by a radical. Adopting the traditional idea of fixed phase prevents a correct analytical expression of the 2D spectrum, which impedes the development of efficient frequency domain-based algorithms for CTSSAR imaging. With this in mind, Sun et al. [16] use a quadratic approximation to the range function to get the spectrum and create an imaging technique. The effect of the curved trajectory may be ignored and satisfactory results obtained if the synthetic aperture is small and the azimuth resolution is low. However, the high-order range components are disregarded by the quadratic approximation approach. In the event that the

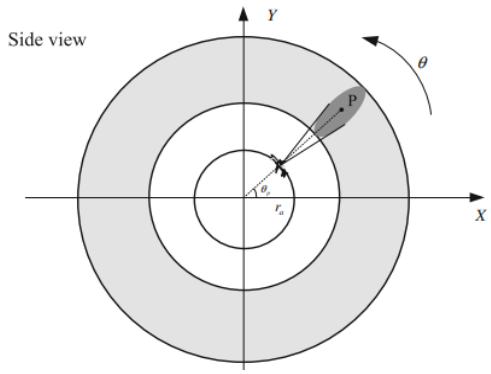

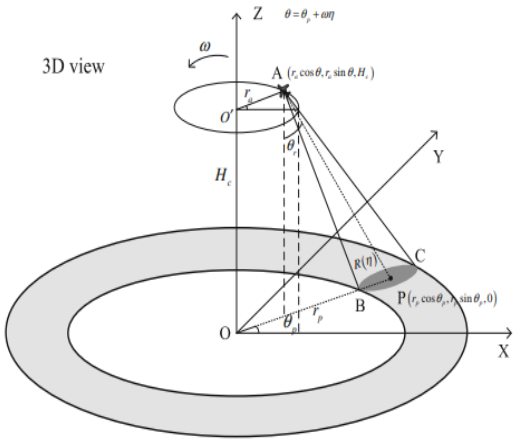

figure 1 Imaging geometry of the CTSSAR

integration time is long and the azimuth resolution is high, the range errors introduced by this approximation will be large enough to defocus the image. The back projection (BP) algorithm shown in [10] is a classical time-domain algorithm, which can get rid of the problem of spectrum derivation in the frequency-domain-based algorithms and be implemented easily with arbitrary geometries. But the disadvantage is that each pixel must be compensated individually, leading to a heavy computational burden.

Signal model for CTSSAR

The imaging geometry for CTSSAR is shown in Figure 1. The radar platform moves along a circular path of radius ran with height Ch on a plane parallel to the ground plane. As the radar moves, its beam is in the plane perpendicular to the flight velocity all the time. When the radar platform moves around a whole circle cantered at the origin point O of the spatial coordinate, the beam-illuminating scene will be an annular area with inner radius OB and outer radius OC. The coordinate of radar platform A is denoted by (ran cos θ, ran sin θ, Hc), where the aspect angle is θ. Assume that there is an arbitrary point target P located at (rp cos θp, rp sin θp, 0). For simplicity of the following derivation, let us define that the slow time is zero when θ = θp, namely, the beam center crossing time. The angle velocity is denoted by ω, and the slow time is represented by η. So, we have θ = θp + ωη. Thus, the instantaneous range R(η) between the radar and the target P can be obtained based on the law of cosines as shown in the following expressions

$$H_c \tan\theta_r = r_p - r_a$$

$$R(\eta) = \sqrt{H_c^2 + r_p^2 + r_a^2 - 2r_a r_p \cos\ (\theta - \theta_p)}$$
$$= \sqrt{H_c^2 + r_p^2 + r_a^2 - 2r_a r_p \cos\omega\eta}$$

Defining

$$R_{\text{cen}} = \sqrt{H_c^2 + (r_p - r_a)^2},$$

we perform Taylor expansion to the instantaneous range neglecting the terms whose order are higher than the fourth order. The expression can be written as

$$R(\eta) = R_{\text{cen}} + k_1\eta + k_2\eta^2 + k_3\eta^3 + k_4\eta^4 + \text{K}$$

Where

$$k_1 = 0, k_2 = \frac{r_a r_p \omega^2}{2R_{\text{cen}}}, k_3 = 0, k_4$$
$$= -\frac{\omega^4 r_a r_p}{24R_{\text{cen}}} - \frac{\omega^4 r_a^2 r_p^2}{8R_{\text{cen}}^3}$$

Assume that the transmitting radar signal is linear frequency modulation signal, the pulse width is Tp, and the rate of frequency modulation is γ. The echo from P can be presented by

$$s_r(t,\eta) = \sigma_p a_r\left[t - \frac{2R(\eta)}{c}\right] a_a(\eta)\cdot\exp\left\{j\pi\gamma\left[t - \frac{2R(\eta)}{c}\right]^2\right\}\cdot\exp$$
$$\times\left[-j\frac{4\pi}{\lambda}R(\eta)\right],$$

where σp is the coefficient of reflectivity, ar(•) and aa(•) are the range envelope and azimuth envelope, respectively, c is the speed of light, and λ is the wavelength according to the center frequency. Now, convert the echo signal shown in (5) to the range frequency azimuth time domain.

$$S_0(f_\tau,\eta) = \sigma_p A_r(f_\tau) a_a(\eta)\cdot\exp\left[-j\frac{4\pi(f_c + f_\tau)R(\eta)}{c}\right]\cdot\exp$$
$$\times\left(-j\frac{\pi f_\tau^2}{\gamma}\right)$$

where fc is the carrier frequency, fτ is the range frequency, and Ar(fτ) represents the envelope of the range frequency. Now let us try to figure out the 2D spectrum using the stationary phase method as follow, first azimuth FFT is performed to (6), yielding

$$S_2(f_\tau, f_\eta) = \int_{-\infty}^{+\infty} S_0(f_\tau,\eta)\exp(-\text{j}2\pi f_\eta\eta)\,\text{d}\eta$$
$$= \int_{-\infty}^{+\infty} \sigma_p A_r(f_\tau) a_a(\eta)\cdot\exp\{\theta(\eta)\}\,\text{d}\eta$$

Simulation results

In SAR imaging, the negligible high-order term error should satisfy the criterion that the maximum double range phase error is less than π/4 rad for the range approximation errors [19]. Herein, it is necessary to select an appropriate approximated order. On one side, if the approximation order is too small, the precision will not be large enough to focus the image data. On the other side, too large an approximation order will surely bring certain extra computation, but it will not be the main computational consumption in the practical use for the reason that it is too small compared with the primary computational operation and it can be precalculated and set in the RAM. Nevertheless, more important is that if higher-order range approximation is adopted, the derivation of the 2D spectrum will become very complex and difficult when using MSR [17], especially for the case that the order is larger than fourth-order, the condition under which it is very complicated for calculating the 2D spectrum. In addition, it is widely accepted that the computational complexity of the time domain BP algorithm is

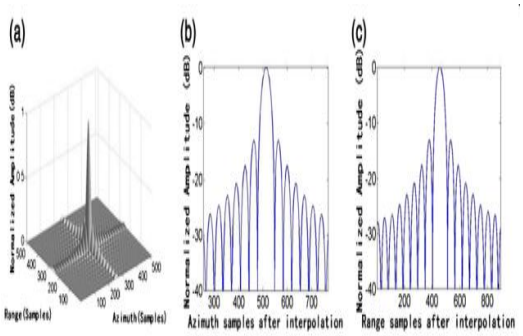

Figure 2 Nearest point imaging result using the proposed method. (a) 2D impulse response. (b) Azimuth impulse response. (c) Range impulse response.

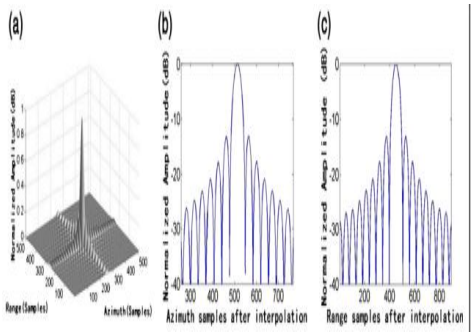

Figure 3 Farthest point imaging result using the proposed method. (a) 2D impulse response. (b) Azimuth impulse response. (c) Range impulse response.

O(N3) [15]. Taking the complex multiplication into consideration, as illustrated in [19], the number of floating point operations (FLOPs) is used here to estimate the computation load of the algorithm. An FFT or IFFT of length N requires 5 N log2(N)FLOPs. A complex phase multiplication requires six FLOPs. It is assumed that Na is the number of input lines (azimuth samples); Nr is the number of input range samples per line. Thus, according to the algorithm flowchart, there are four FFT (or IFFT) operations and two complex multiplication operations:

$$N_{\text{total}} = 5N_rN_a\log_2(N_r) \times 3 + 6N_rN_a \times 2 + 5N_rN_a\log_2(N_a)$$

Therefore, let Nr = Na = N, the computational complexity of our algorithm is O(N2 log2(N)), which is a tremendous improvement for the computational efficiency. In the following simulation, corresponding computational processing time experiments will be carried out with related analyses. Now let us discuss how large the order is needed to satisfy the request of imaging quality. Here, we choose a series of typical parameters. Assume that the parameters of the flight platform are Hc = 2000 m, ra = 4000 m, rp = 5154.7 m, v = 100 m/s, and the wavelength λ = 0.03 m, now compute the quadratic approximation errors and the quartic approximation errors in one synthetic aperture, as shown in Figures 3 and 4, respectively. The dashed line denotes the location when the phase error is π/4 rad, and the solid line indicates the phase errors introduced by different range approximations in the integrated synthetic aperture time.

Besides, the cubic approximation errors are not considered here for the fact that the odd terms are all zero. It can be seen clearly from the figure that the maximum value of the quadratic approximation errors is about 1.7 rad, larger than π/4 rad indicated by the dashed line in the figure, which implies that the approximated errors introduced by quadratic approximation cannot be ignored, or the degradation of the image focusing may occur. However, the maximum quadratic approximated errors is about 3 × 10–3 rad, far less than π/4 rad, so the dashed line does not noted in the figure. Thus, it is obvious that the expression in (15) is more applicable than the quadratic approximated one. In order to verify the effectiveness of the proposed algorithm in this article, let us compare our algorithm with the quadratic approximation method in terms of image quality. The simulation parameters are shown in Table 1, there are three target points Pn, Pm, and Pf in the scene, and their coordinates are Pn(0, 4854.7, 0), Pm (0, 5154.7, 0), and Pf(0, 5454.7, 0), respectively. The imaging results of the two algorithms for the same scene center point is shown in Figures 5 and 6 to compare the two algorithms, where (a) is the 2D impulse response of the target point, (b) is the azimuth impulse response, and (c) is the range impulse response. From the figure, we can see that the quadratic approximation is not able to represent the enough phase variant information and the focusing is not satisfied. In contrast, the algorithm proposed in this article keeps the range up to fourth-order and presents more range-variant information in the 2D frequency domain. So, it is possible to

table 2 Image quality parameters using the proposed method

Parameter	Theoretical one		P_n		P_m		P_f	
	Azimuth	Range	Azimuth	Range	Azimuth	Range	Azimuth	Range
Resolution (m)	0.125	0.443	0.126	0.443	0.126	0.445	0.126	0.443
PSLR (dB)	−13.26		−13.22	−13.29	−13.25	−13.26	−13.69	−13.28
ISLR (dB)	−9.8		−9.83	−9.83	−9.88	−9.85	−9.94	−9.89

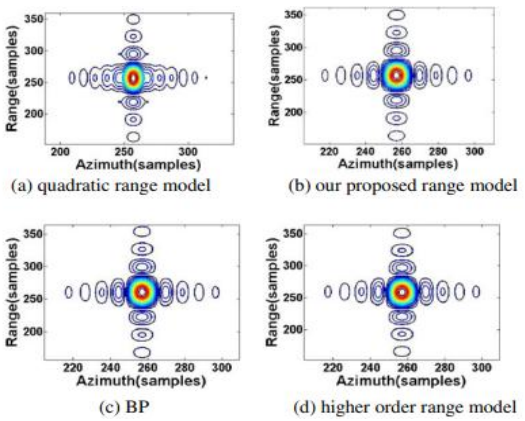

Figure 4Comparison of different imaging method for a selected point target. (a) Quadratic range model. (b) Our proposed range model. (c) BP. (d) Higher-order range model

have access to the accurate image with high resolution. Figures 7 and 8 are the imaging results of the nearest point and the farthest point using our method, respectively. It is obvious that not only the center point, but also other points in different range are all well focused, which prove the feasibility of the proposed method successfully. Table 2 lists the image quality parameters to the three points of our algorithm. Besides, the theoretical range resolution and azimuth resolution are 0.443 and 0.125 m, respectively [16]. It can be seen from Table 2 that each parameter is close to the theoretical one, which indicates satisfactory imaging results and further validates the effectiveness and feasibility.

To further illustrate the superiority of the proposed algorithm over other imaging methods, some imaging results are provided and computational experiments are implemented here. Figure 9 indicates the contour plots of different imaging method for a selected point target Pm, where Figure 9a delineates the imaging result for the quadratic range approximated algorithm, Figure 9b shows the contour of the proposed algorithm based on quartic range approximation, Figure 9c represents the result of BP algorithm, and Figure 9d is the image for higher-order range approximation (sixth-order is used here). It is obvious that the quadratic approximation is not precise enough to focus the image in CTSSAR and the time domain BP algorithm seems to be trusted to

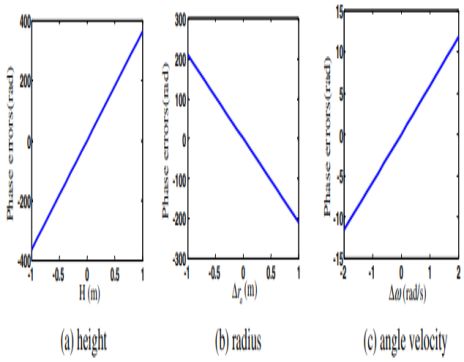

Figure 5 Phase errors caused by each parameter errors. (a) Height. (b) Radius. (c) Angle velocity

do this to perfection. However, it is challenging to apply to real engineering usage because of the excessive computing burden. In contrast, our suggested approach can get access to a perfect outcome while still being very efficient computationally. The picture obtained using a higher-order approximation is sharp, but it scarcely outperforms the one shown in Figure 9b. It thus seems that an additional higher-order approximation is not required in CTSSAR processing, confirming the correctness of our estimate. In addition, the difficulty in deriving the 2D spectrum increases with the estimated order. The computational loads are assessed to verify our algorithm's computational efficiency. The time domain BP methodology takes 14676.80 seconds to run in our experiment, whereas our suggested algorithm takes just 40.43 seconds, and the higher-order approximation method (here, we utilize sixth-order approximation to simulate) takes 48.58 seconds. Figure 9a displays the clearly defocused result achieved using the quadratic approach, which only takes 26.67 s. Since the BP algorithm is too slow for imaging, the quad ratic method is inadequate, and the higher-order method takes slightly longer than the proposed method (though the procedure can be optimized in practice, as was previously mentioned), it is clear that the proposed method is superior. The higher-order approximation also introduces significant computational challenges to the MSR-based 2D spectrum derivation. After looking at how the suggested algorithm stacks up against other common imaging techniques, it is clear that it is the best option for CTSSAR.

Conclusions

The CTSSAR imaging geometry model is initially constructed in this article, followed by the disclosure of imaging challenges and impediments. Next, MSR deduces the point target range function and its 2D frequency spectrum, analyzes the estimated phase errors, and verifies the result with relevant tests, all while providing a solution to the challenge of selecting the approximation order. The generated spectrum is used to inform the development of a refined Omega-K technique. In order to account for the high-order term that the circular track introduces, the algorithm begins with a compensation. Sub-images are created by first performing range compression and RCMC in the 2D domain, then azimuth compression, and then combining all of the obtained sub-images to create the final picture. The suggested approach is more precise than the quadratic approximation method. The simulation tests towards the article's conclusion verify the practicability and efficacy of the suggested strategy.

References

[1]. RK Raney, H Runge, R Bamler, IG Cumming, FH Wong, Precision SAR processing using chirp scaling. IEEE Trans. Geosci. Remote Sens. 32, 786–799 (1994)

[2]. N Gebert, G Krieger, Azimuth phase center adaptation on transmit for highresolution wide-

swath SAR imaging. IEEE Geosci. Remote Sens. Lett. 6, 782–786 (2009)

[3]. C Cafforio, C Prati, F Rocca, SAR data focusing using seismic migration techniques. IEEE Trans. Aeorsp. Electron. Syst. 27, 194–207 (1991)

[4]. M Soumekh, Synthetic Aperture Radar Signal Processing With Matlab Algorithms (Wiley, New York, 1999

[5]. K Knaell, Three-dimensional SAR from curvilinear apertures. Proceedings of IEEE Radar Conference, Carderock Div 2230, 220–225 (1996). NSWC, Bethesda, MD, USA

[6]. D Falconer, G Moussally, Tomographic imaging of radar data gathered on a circular flight path about a three-dimensional target zone. Proceedings of SPIE, Aerosp, Syrup 2487:2–12 (1995). Orlando, FL

[7]. A Ishimaru, T Chan, Y Kuga, An imaging technique using confocal circular synthetic aperture radar. IEEE Trans. Geosci. Remote Sens. 36, 1524–1530 (1998)

[8]. M Bara, L Sagues, F Paniahua, A Broquetas, X Fabregas, High-speed focusing algorithm for circular synthetic aperture radar. Electron. Lett. 36, 828–830 (2000)

[9]. H Cantalloube, EC Koeniquer, Airborne SAR imaging along a circular trajectory, in (Proceedings of EUSAR, Dresden, Germany, 2006), pp. 16–19

[10]. H Cantalloube, EC Koeniquer, H Oriot, High resolution SAR imaging along circular trajectories (Proceedings of IGARSS, Spain, Barcelona, 2007), pp. 850–853

[11]. M Soumekh, Reconnaissance with slant plane circular SAR imaging. IEEE Trans. Image Process. 5, 1252–1265 (1996)

[12]. M Ferrara, JA Jackson, C Austin, Enhancement of multi-pass 3D circular SAR images using sparse reconstruction techniques, in. Algorithms for Synthetic Aperture Radar Imagery XVI, Proceedings of SPIE 7337, 733702 (2009). Orlando, FL

[13]. M Pinheiro, P Prats, R Scheiber, M Nannini, A Reigber, Tomographic 3D reconstruction from airborne circular SAR. Proceedings of IGARSS 3, III21–III24 (2009). Cape Town, South Africa

[14]. Y Lin, W Hong, WX Tan, YR Wu, Extension of range migration algorithm to squint circular SAR imaging. IEEE Geosci. Remote Sens. Lett. 8, 651–655 (2011)

[15]. B Sun, YQ Zhou, J Chen, CS Li, Operation mode of circular trace scanning SAR for wide observation. J. Electron. Inf. Technol. 30, 2805–2808 (2008)